



Available online at www.sciencedirect.com

ScienceDirect

Geochimica et Cosmochimica Acta 254 (2019) 156-172

Geochimica et Cosmochimica Acta

www.elsevier.com/locate/gca

A high carbon content of the Hawaiian mantle from olivine-hosted melt inclusions

Jonathan M. Tucker^{a,*}, Erik H. Hauri^{a,1}, Aaron J. Pietruszka^b, Michael O. Garcia^c, Jared P. Marske^{a,2}, Frank A. Trusdell^d

^a Carnegie Institution for Science, Washington, DC 20015, USA

^b U.S. Geological Survey, Denver Federal Center, Denver, CO 80225, USA

^c University of Hawaii, Honolulu, HI 96822, USA

^d U.S. Geological Survey, Hawaiian Volcano Observatory, Hawaii Volcanoes National Park, HI 96718, USA

Received 2 November 2018; accepted in revised form 1 April 2019; available online 6 April 2019

Abstract

The deep mantle carbon content and flux are fundamental quantities in understanding global volatile cycles and distributions. Here, we present CO₂ concentrations measured in 407 olivine-hosted melt inclusions from Hualalai, Kilauea, Koolau, Loihi, and Mauna Loa to constrain the Hawaiian mantle CO₂ content and flux. Quantification of melt inclusion CO₂ is complicated by the ubiquitous presence of vapor or "shrinkage" bubbles. The contribution from exsolved shrinkage bubble CO₂ was determined from the measured bubble size and a CO₂ equation of state, and added to the dissolved CO₂ to reconstruct total melt inclusion CO₂ concentrations. Bubbles typically contain ~90% of melt inclusion C, much of which may be sequestered in precipitated phases on bubble walls, and thus not amenable to measurement by Raman spectroscopy. Based on our dataset of total (dissolved + bubble) CO₂ concentrations, we estimate that parental melts from the five Hawaiian volcanoes have CO₂ concentrations ranging from 3900 to 10,000 ppm CO₂. Among the active volcanoes, CO₂ concentrations decrease to the northwest, likely reflecting mantle source heterogeneity, although differences in CO₂ degassing related to the relative depths of the magma chambers may also play a role. Mantle sources of the Hawaiian volcanoes range from 380 to 480 ppm CO₂ suggesting that the Hawaiian plume is at least a factor of ~4 more C-rich than the upper mantle sampled by mid-ocean ridge basalts. This enrichment is likely due to the presence of recycled surficial C and/or C-rich primitive material in the Hawaiian mantle.

© 2019 Elsevier Ltd. All rights reserved.

Keywords: Hawaii CO2 flux; Mantle carbon content; Melt inclusions; Shrinkage bubbles

1. INTRODUCTION

The volcanic flux of carbon from the mantle to the surface is a critical aspect of global volatile cycles (e.g.

Dasgupta and Hirschmann, 2010; Kelemen and Manning, 2015) and the dominant control of long-term climate (Walker et al., 1981; Sleep and Zahnle, 2001). Whereas subduction-related volcanism predominantly erupts surficial carbon recycled through subduction zones (Sano and Williams, 1996; Mason et al., 2017), mid-ocean ridge basalts (MORB) and ocean island basalts (OIB) may erupt primitive mantle carbon or ancient carbon that has been deeply subducted into the mantle. Consequently, robust constraints on carbon fluxes from MORB and OIB are

 $^{^{}st}$ Corresponding author.

E-mail address: jtucker@carnegiescience.edu (J.M. Tucker).

Deceased.

² Current address: Los Alamos National Laboratory, Los Alamos, NM 87544, USA.

essential for decoding the deep carbon cycle, and the Earth's total carbon content. The upper mantle sampled by MORB is well characterized to have ~100 ppm CO₂, corresponding to a CO₂ flux on the order of 100 Tg/year (Michael and Graham, 2015; Rosenthal et al., 2015; Hauri et al., 2018; Tucker et al., 2018). However, the carbon contents of deep mantle domains sampled by OIB, and their corresponding CO₂ fluxes, are poorly known. Hawaii, in particular, produces the largest modern oceanic intraplate magmatic flux and is rooted in the lower mantle (Montelli et al., 2004; Wolfe et al., 2009; French and Romanowicz, 2015).

OIB magmas are typically subject to extensive degassing of insoluble magmatic volatiles like CO2 because they are stored and erupt at relatively low pressure. This irreversible loss of volatiles renders estimates of pre-degassing CO₂ concentrations, total CO2 fluxes, and mantle source CO2 concentrations problematic. Pre-degassing CO₂ concentrations in Hawaiian magmas have been estimated from maximum measured values in vesicular basalts (Dixon and Clague, 2001), application of degassing models (Gonnermann and Mukhopadhyay, 2007), and measurements of volcanic CO₂ emissions (Gerlach et al., 2002; Anderson and Poland, 2017), although each of these methods has potential difficulties. Maximum measured values are not particularly robust statistics, especially for a small sample set, and assume that bubbles have not been added or lost from host magmas. Degassing model results can depend strongly on poorly constrained physical parameters, such as C diffusivity. Emissions monitoring is spatially and temporally restricted, for example, to Kilauea, among the active Hawaiian volcanoes.

Another methodology to constrain pre-degassing CO₂ concentrations is to exploit small droplets of melt trapped inside primitive olivine crystals. These olivine-hosted melt inclusions can document an earlier and less degassed stage of magmatic evolution than erupted basalts (Sobolev, 1996). In some cases, melt inclusions have been argued to preserve undegassed magmas (Saal et al., 2002; Le Voyer et al., 2017; Hauri et al., 2018). However, previous studies of Hawaiian melt inclusions have only found inclusions that experienced pre-entrapment degassing (Hauri, 2002; Edmonds et al., 2013; Sides et al., 2014a,b).

Melt inclusions are subject to various forms of postentrapment modification, including formation of a vapor or "shrinkage" bubble, a common feature of melt inclusions from all tectonic environments (e.g. Roedder, 1984; Moore et al., 2015; Maclennan, 2017). Shrinkage bubbles nucleate and grow when the solubility of CO₂ in the melt drops below the saturation limit. Three effects resulting from post-entrapment cooling may cause CO₂ solubility to drop: differential thermal contraction of melt and host olivine (Roedder, 1984; Lowenstern, 1995), reduction of the melt volume by post-entrapment crystallization (Roedder, 1984; Steele-Macinnis et al., 2011), and changing melt compositions during post-entrapment crystallization (Maclennan, 2017). Because the bubble may host a significant fraction of an inclusion's CO2, measurement of exsolved CO2 in the bubble, in addition to dissolved CO2

in the glass, is required to determine the total CO₂ concentration of a melt inclusion.

A number of methods have been used to attempt to quantify CO_2 concentrations in shrinkage bubbles, including heating the melt inclusions to re-dissolve shrinkage bubbles (e.g. Hauri, 2002; Mironov et al., 2015; Wallace et al., 2015; Tuohy et al., 2016), measurement of bubble CO_2 density by Raman spectroscopy, (e.g. Esposito et al., 2011; Hartley et al., 2014; Moore et al., 2015; Aster et al., 2016), and calculation of bubble CO_2 density by an equation of state (Shaw et al., 2008, 2010; Wanless and Shaw, 2012; Wanless et al., 2014, 2015; Moore et al., 2015; Hauri et al., 2018). These studies generally find that the majority (\sim 50–90%) of melt inclusion CO_2 is sequestered in the bubble. Thus, it is essential to account for the CO_2 budget of the bubble to capture the total melt inclusion CO_2 concentration.

Here, we apply the equation of state method to a large set of Hawaiian melt inclusions with the goals of constraining pre-degassing CO_2 concentrations and quantifying the CO_2 flux and mantle source CO_2 content of the Hawaiian plume. We explore the possible causes of variability in CO_2 contents between the active Hawaiian volcanoes and compare the Hawaiian results with MORB magma and source CO_2 contents.

2. SAMPLES AND METHODS

2.1. Sample descriptions

We measured 437 individual olivine-hosted melt inclusions from 29 samples from 5 Hawaiian volcanoes (Fig. 1): Loihi (84 inclusions from 7 samples), Kilauea (167 inclusions from 9 samples), Mauna Loa (137 inclusions from 10 samples), Hualalai (35 inclusions from 2 samples), and Koolau (14 inclusions from 1 sample). Major and trace element compositions of melt inclusions, as well as inclusion-proximal olivine, were measured by laserablation ICP-MS (Marske and Hauri, 2019). The melt inclusions are hosted in olivine crystals ranging from Fo₈₂₋₉₁, with an average of Fo₈₈. Melt inclusions span a wide range of sizes, most having maximum diameters between 50 and 400 µm (Table S1). Shrinkage bubbles were frequently observed, although in many cases were partly or completely polished away to reveal sufficient area $(\sim 100 \, \mu \text{m})$ for chemical analysis of the melt inclusion glass. Thus, we cannot distinguish between cases where a bubble was polished away or never existed. Example melt inclusion photomicrographs are shown in Fig. 2.

2.2. CO₂ measurements and the equation of state method

The total CO_2 concentration in a melt inclusion is the sum of the dissolved CO_2 in the melt (CO_2^d) and the exsolved CO_2 in the bubble. The concentration of CO_2 in the bubble at any time during its growth is $\phi \times \rho_v/\rho_m$, where ϕ is volume fraction of the bubble in the melt inclusion, ρ_v is the volumetric CO_2 vapor density, and ρ_m is the melt density, calculated from the glass composition. Conse-

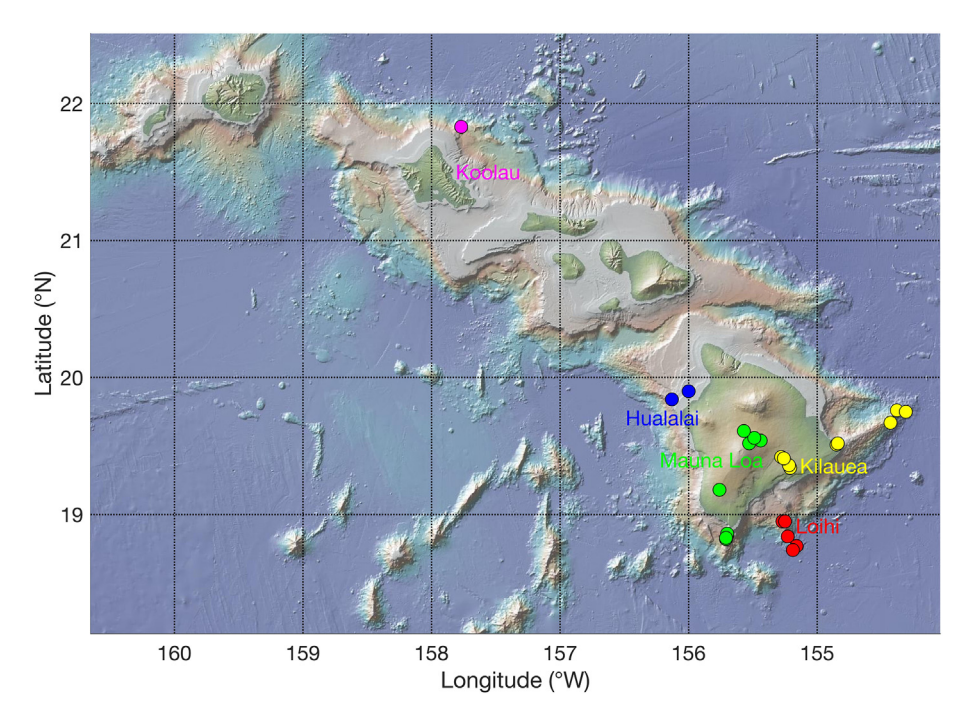


Fig. 1. Map of the Hawaiian volcanoes and samples in this study. Sample locations provided in Table S1. Bathymetry is from Global Multi-Resolution Topography synthesis (www.gmrt.org; Ryan et al., 2009).

quently, the total (dissolved + bubble) CO_2 concentration in ppm is

$$CO_2^{total} = CO_2^d + \phi \frac{\rho_v}{\rho_m} \times 10^6 \tag{1}$$

Rather than measuring ρ_v directly in the bubble (see Section 4), the basis of the equation of state method is to calculate ρ_v using a CO₂ equation of state from the temperature and pressure at which the bubble size was fixed. We assume that the bubble ceases to grow once the melt cools to a temperature of 725 °C (i.e. the glass transition temperature determined for Kilauea tholeiitic basalts; Ryan and Sammis, 1981). We also assume that equilibrium is maintained between the melt and vapor, so that the internal pressure of the melt inclusion, as well as the CO₂ fraction in a mixed CO₂-H₂O vapor, can be calculated from a CO₂-H₂O solubility model (Dixon et al., 1995) and the dissolved CO₂ and H₂O concentrations. We then use the CO₂ vapor equation of state of Duan and Zhang (2006) to calculate ρ_v from the pressure and temperature. However, we explore the assumption of equilibrium and our choices of solubility model and equation of state in Section 2.3. Dissolved CO₂ concentrations (CO₂^d) were determined by SIMS analysis (Marske and Hauri, 2019). Total CO₂ concentrations for all melt inclusions calculated via Equation (1), as well as the intermediate quantities required, are listed in Table S1.

The bubble volume fraction ϕ was calculated by measuring the melt inclusion and bubble sizes photomicrographically (Fig. 2b). In nearly all cases, bubbles appeared spherical, but were occasionally ellipsoidal. In many cases, the full diameter of vapor bubbles was visible, so they were measured at their widest part. In others, the bubble was polished below its widest part, so ϕ , and consequently total

CO₂ concentration, are lower limits. Melt inclusion sizes are more problematic because depths cannot be reliably measured optically from polished surfaces. Therefore, melt inclusions were assumed to be triaxial ellipsoids with the third axis normal to the polished plane equal to the average of the measured long and short axes. The uncertainty associated with this assumption is explored in Section 2.3.1. Irregularly shaped melt inclusions (e.g. Fig. 2d) could not be measured accurately and were not included in this study.

Spinel inclusions were commonly observed inside the olivine crystals, and occasionally observed within the melt inclusions, usually at their edges (e.g. Fig. 2c,d). If the crystals within the melt inclusion formed from the parental magma, rather than as daughter minerals from the melt inclusion, their volume should be excluded from the melt inclusion. Not excluding such crystals from the melt inclusion volume results in an underestimate of ϕ and consequently total CO₂ concentration.

 CO_2 concentrations were corrected for post-entrapment crystallization by adding or subtracting olivine in 0.1% mass increments until the melt inclusion Mg# was in equilibrium with the host olivine Mg#. Corrections are typically on the order of 5–10% (Table S1). Some melt inclusions were too small for LA-ICPMS analysis ($<\!\!\sim\!\!100~\mu m$ diameter), in which cases we assumed the extent of post-entrapment crystallization was equal to the average of that of the other melt inclusions from the same sample.

2.3. Uncertainties in total CO₂ concentrations

The major sources of uncertainty in reconstructing total CO_2 concentrations are uncertainty in the bubble volume fraction ϕ resulting from the unknown third melt inclusion

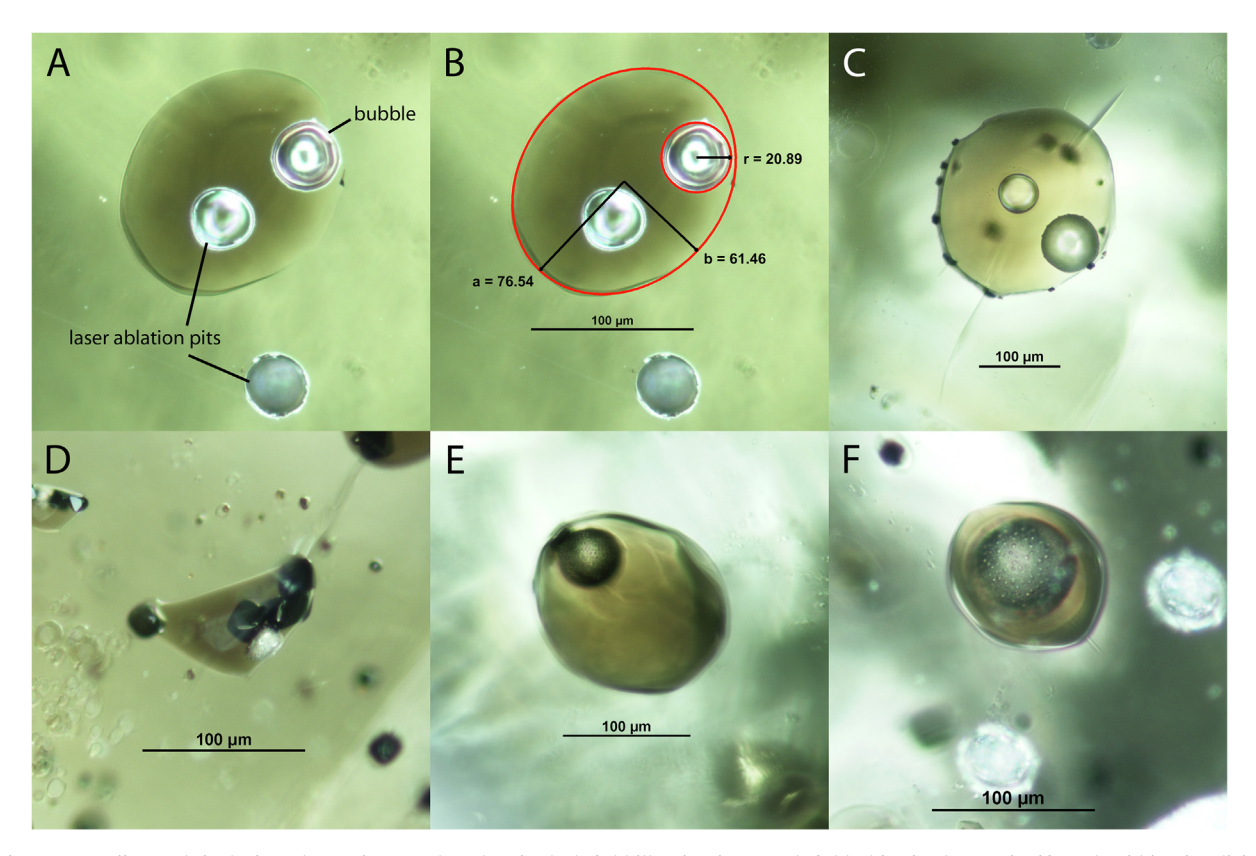


Fig. 2. Hawaiian melt inclusion photomicrographs taken in dark field illumination. Dark field objective lenses significantly aid in visualizing below the polished surface. (A, B) Kilauea melt inclusion Kil-2012-8_4a showing fitted inclusion and bubble dimensions. Measurements were made using Nikon NIS-Elements D software. (C) Mauna Loa melt inclusion ML2-1_38a showing spinel crystals around the inclusion rim. These crystals do not significantly affect measurement of the melt inclusion or bubble dimensions. (D) Melt inclusion from Kilauea sample Kil-2011-4 which could not be measured due to irregular shape and large spinel crystals. (E) Melt inclusion from Kilauea sample Kil3-6 (not measured), and (F) Loihi melt inclusion 6K491-2_11b, containing bubbles not exposed by polishing. The photographs are focused on the upper bubble surfaces, revealing bumpy textures, possibly indicative of carbon-bearing phases precipitated from the CO₂ vapor (Section 4; Fig. 11). Similar textures are seen on the majority of bubble surfaces, but not visible in panels A-C because the photographs are focused at the polished surface. The bubble in panel (F) comprises 27% of the melt inclusion volume, and may be a trapped magmatic bubble rather than a shrinkage bubble.

dimension, and uncertainty in ρ_v resulting from the possibility of nonequilibrium bubble expansion, the solubility model, and equation of state, as discussed below.

2.3.1. Bubble volume fraction

Measurement of the melt inclusion volume is required to determine the bubble volume fraction ϕ (Eq. (1)). Once an olivine crystal is polished to expose a melt inclusion, the inclusion generally appears as an ellipse, and information about the third dimension, and consequently the melt inclusion volume, is lost. Many studies assume an ellipsoidal melt inclusion geometry where the length of the third semi-axis c (normal to the polished plane) equals the smaller of the two visible dimensions: a > b = c (Shaw et al., 2008, 2010; Wanless and Shaw, 2012; Hartley et al., 2014; Neave et al., 2014; Wanless et al., 2014, 2015; Rasmussen et al., 2017; Hauri et al., 2018). Other studies assume the third dimension equals the arithmetic mean (Moore et al., 2015) or the geometric mean (Ni et al., 2017) of the two visible axes. However, the melt inclusion orientation was not

determined before polishing; thus, the third semi-axis is not known.

To explore the uncertainty associated with an assumed third semi-axis, we compared actual volumes to volumes calculated using assumed third semi-axis lengths in a set of simulated melt inclusions. We generated 106 randomly sized triaxial ellipsoids, representing melt inclusions of different sizes. One example is shown in Fig. 3a. The ellipsoids were intersected by randomly oriented planes, resulting in ellipses of intersection (Fig. 3a,b), simulating polished surfaces of randomly oriented melt inclusions. The volumes of the original ellipsoids were then compared to the volume calculated under three assumptions: that the third axis of the ellipsoid c equals (1) the smaller of the two visible axes (c = b), (2) the arithmetic mean of the two visible axes (c =(a+b)/2), and (3) the geometric mean of the two visible axes $(c = \sqrt{ab})$. Fig. 3c shows the distribution of errors in computed volumes under these three assumptions. The relative error associated with each assumed volume calculation can be quite large for any of the three assumptions

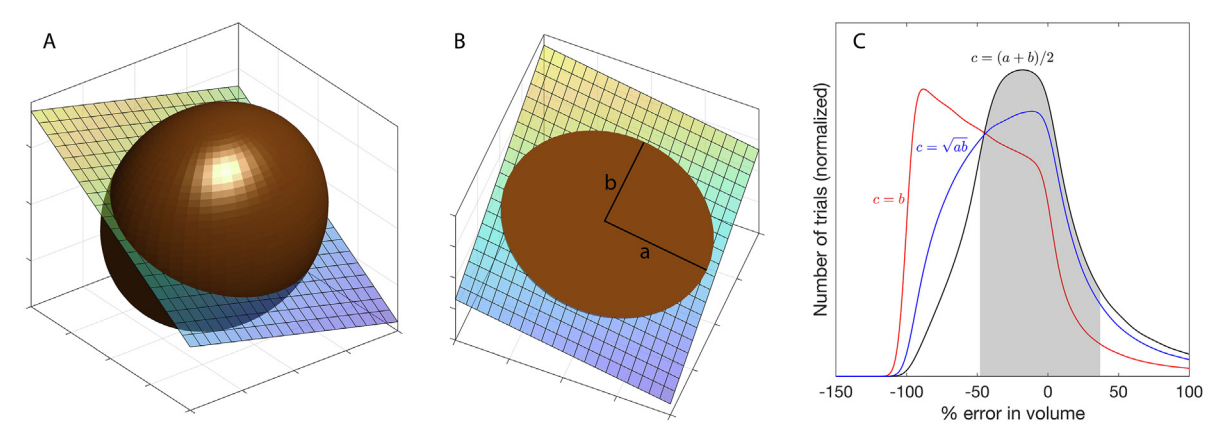


Fig. 3. Uncertainty resulting from melt inclusion geometry. (A) Example of a randomly oriented triaxial ellipsoid, representing a melt inclusion, and a planar slice representing a polished surface. (B) Rotated view of (A). The plane intersects the ellipsoid in an ellipse, obscuring information about the third dimension. Consequently, any assumption about the size of the third dimension may induce significant error in the calculated melt inclusion volume. "a" and "b" are the long and short visible axes, respectively. (C) Probability distribution estimates of relative error in simulated melt inclusion volume under three different assumptions: the third (invisible) axis equals the smaller visible axis (red); the visible axes' arithmetic mean (black); and the geometric mean (blue). Distributions are calculated from 10⁶ randomly sized and oriented triaxial ellipsoids; one such example shown in panels A and B. The arithmetic and geometric mean assumptions most closely approximate the true volume; the arithmetic mean is used in this study. Assuming the third axis equals the smaller visible axis, most common in the literature, tends to underestimate inclusion volume and consequently overestimate total CO₂ concentrations. (For interpretation of the references to colour in this figure legend, the reader is referred to the web version of this article.)

(Fig. 3c). Assumption (1), commonly used in the literature, almost always underpredicts the melt inclusion volume (by 36% on average), and consequently can greatly overpredict the total melt inclusion CO_2 concentration. The average errors in assumptions (2) and (3) are only 5% and -9%, respectively, indicating that these assumptions more often approximate the true value. The arithmetic mean assumption is used in this study because its error distribution most closely resembles a Gaussian distribution; however, the error associated with this assumption is still large: the middle 68% range of the error distribution is -48% to 37% (shaded region of Fig. 3c).

2.3.2. Nonequilibrium bubble expansion

The equation of state method calculates ρ_v under the assumption that a bubble and melt remain in equilibrium until the bubble ceases to expand at the glass transition temperature (Section 2.2). However, because diffusivity is temperature dependent, C diffusion may effectively cease at a temperature higher than the glass transition temperature, resulting in bubble expansion without C exsolution (e.g. Maclennan, 2017). This nonequilibrium expansion would decrease the CO₂ vapor density ρ_v , resulting in an overestimation of ρ_v and the total inclusion CO₂ concentration by the equation of state method. Consequently, the estimates of ρ_v and total inclusion CO₂ concentrations presented here, as well as other studies that use an equation of state method, may be regarded as upper limits.

To assess the likelihood of nonequilibrium bubble expansion, we can explore the conditions under which it might occur. The cessation of C equilibration can be approximated by a diffusive closure temperature; a closure temperature higher than the glass transition temperature implies a stage of nonequilibrium bubble expansion

(Maclennan, 2017). Fig. 4 shows contours of C closure temperatures calculated as functions of cooling rate and diffusive length scale, for two different C diffusion models. Faster cooling (e.g. inclusions from tephra) or longer diffusive length scales result in higher closure temperatures and susceptibility to nonequilibrium bubble expansion, whereas slower cooling (e.g. inclusions in lava flows) or shorter diffusive length scales imply lower closure temperatures and sustained equilibrium throughout bubble growth.

However, significant uncertainties persist in using the type of calculation in Fig. 4 to assess whether nonequilibrium bubble expansion has occurred. For example, the diffusive length scale would be shorter than the radius of the melt inclusion if the melt were mechanically stirred due to bubble growth or movement through the melt, significantly diminishing the likelihood of nonequilibrium bubble expansion (Fig. 4). Additionally, the cooling rates and diffusive length scales required to maintain equilibrium are vastly different between the two diffusion models shown in Fig. 4. While we will argue that the CO₂ concentrations obtained in this study are unlikely to be significantly overestimated (Section 3.4), and that one line of evidence for nonequilibrium bubble expansion may have an alternative explanation (Section 4), more work is required to develop strategies to identify inclusions that have maintained equilibrium throughout bubble growth.

2.3.3. Bubble formation pressure

The partitioning of volatiles (CO_2 , H_2O) between a shrinkage bubble and melt inclusion glass is a strong function of the inclusion pressure, because volatiles become more insoluble at lower pressure. Consequently, the pressure of the inclusion can be determined from the measured CO_2 and H_2O concentrations in the melt inclusion glass and

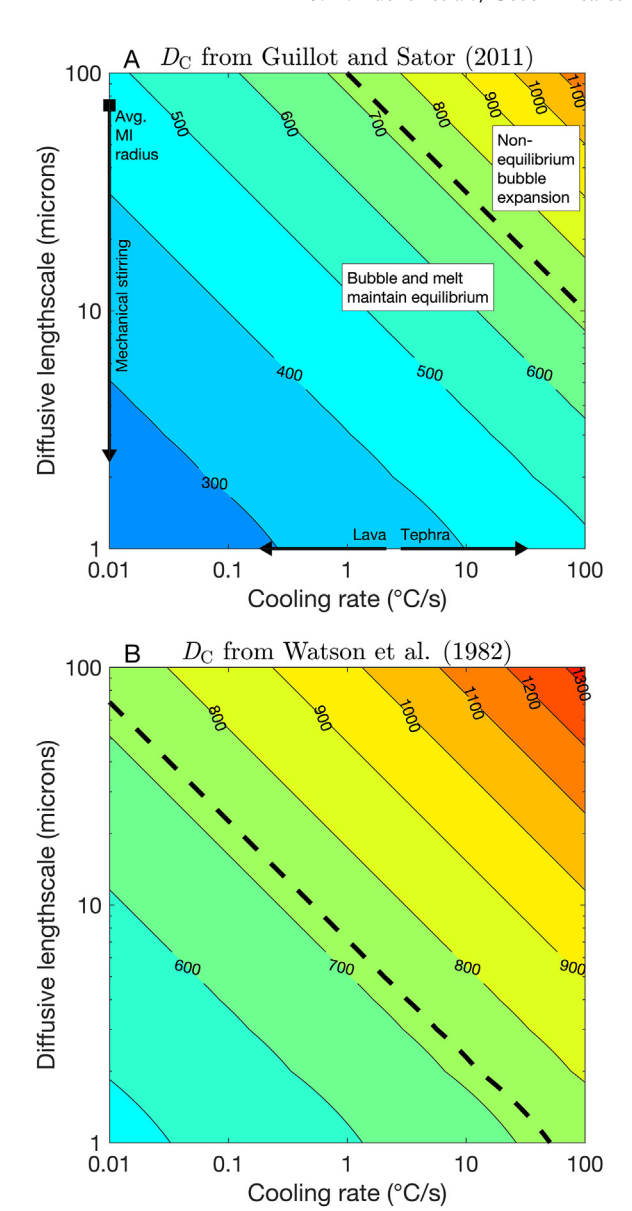


Fig. 4. Contours of C closure temperature as a function of cooling rate and diffusive length scale. A closure temperature higher than the glass transition temperature of 725 °C (dashed line) implies a stage of nonequilibrium bubble expansion and overestimation of ρ_v and total CO_2 by the equation of state method. Inclusions experiencing slower cooling rates (e.g. from lava flows) or shorter diffusive length scales (e.g. from mechanical mixing of the melt via bubble growth and movement) are more likely to maintain bubblemelt equilibrium. Panel A uses an Arrhenius relation fitted to the 20 kbar MORB diffusivities from Guillot and Sator (2011): $E_A = 105.6 \text{ kJ/mol}$, $\ln(D_0) = -14.07 \text{ m}^2/\text{s}$. Panel B uses the C diffusivity model of Watson et al. (1982). Closure temperatures are calculated using the equation of Dodson (1973) assuming a spherical geometry. Lava and tephra cooling rate estimates (Newcombe et al., 2014) are shown for reference.

a volatile solubility model. A number of joint CO₂-H₂O solubility models for basaltic compositions have been published (e.g. Dixon et al., 1995; Iacono-Marziano et al., 2012; Shishkina et al., 2014). The model of Dixon et al.

(1995), which accurately predicts MORB saturation pressures (Le Voyer et al., 2019), is used here, although error in the solubility model may add a systematic uncertainty to total CO₂ concentrations.

2.3.4. Equation of state

Two equations of state were investigated for calculating the vapor density ρ_{ν} from the bubble equilibration pressure and temperature: a high-pressure CO₂ fluid equation of state (Duan and Zhang, 2006), and the ideal gas law, which has been used in many previous shrinkage bubble studies (Shaw et al., 2008, 2010; Wanless and Shaw, 2012; Neave et al., 2014; Wanless et al., 2014, 2015; Moore et al., 2015; Hauri et al., 2018). A high-pressure equation of state may be more applicable because CO₂ is a supercritical fluid above 73 bar. The solubility model predicts a very low H₂O fugacity in the fluid phase (<10% for 2/3 of samples, Table S1), so the effect of H₂O on the CO₂ equation of state was not considered.

The ideal gas law systematically overestimates fluid densities and would consequently overestimate bubble CO_2 contents (Fig. 5). The magnitude of effect increases from a few percent to tens of percent in the highest-pressure bubbles (~ 1000 bar). Consequently, the high-pressure equation of state is used in this study. The ideal gas law may provide an adequate approximation of fluid density at lower bubble formation pressures ($<\sim 200$ bar), but should not be used for bubbles formed at higher pressures.

2.3.5. Summary of uncertainties

The uncertainty in the bubble volume fraction ϕ dominates over all other quantifiable uncertainties, resulting in errors of tens of percent (Fig. 3c). This large uncertainty is generally not taken into account in studies of shrinkage bubble sizes and is applicable either when ρ_v is determined by an equation of state or by Raman spectroscopy (see Sec-

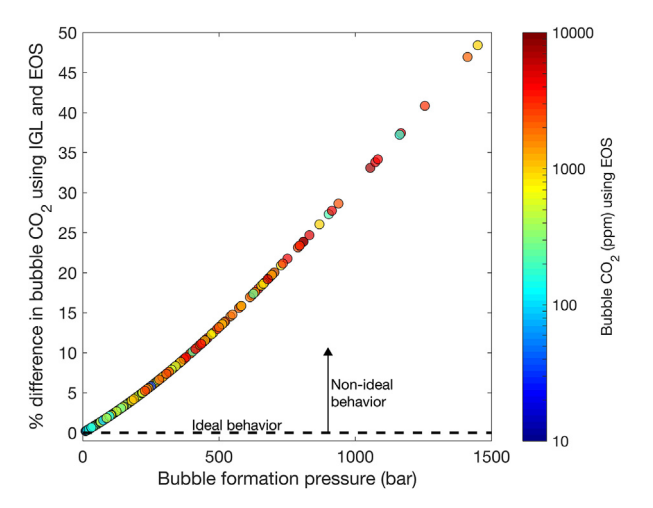


Fig. 5. Comparison of bubble melt inclusion CO_2 concentrations using the ideal gas law (IGL) and a high-pressure CO_2 equation of state (EOS; Duan and Zhang, 2006), colored by total melt inclusion CO_2 using the equation of state. The ideal gas law, often used in the literature, systematically overestimates bubble CO_2 concentrations by up to $\sim 50\%$ for the highest-pressure bubbles.

tion 4). However, it could be mitigated by determination of the bubble and melt inclusion volumes prior to polishing by a method like x-ray microtomography. Analytical uncertainties of a few percent are small compared to the uncertainty in ϕ . Uncertainties associated with the solubility model, bubble closure temperature, and equation of state are likely to be systematic rather than random. Therefore, based on the error distribution of ϕ (Fig. 3c), we conservatively assign a 50% (1 σ) uncertainty to each melt inclusion volume, and propagate this uncertainty to the total CO₂ concentration, resulting in 1 σ uncertainties between 40 and 50% for most samples (Table S1). However, the total CO₂ concentrations represent an upper limit if nonequilibrium bubble expansion has occurred.

3. RESULTS

3.1. Bubble sizes

The distribution of bubble volume fractions ϕ is strongly peaked around 3% (Fig. 6), similar to previous measurements in Hawaiian melt inclusions (Moore et al., 2015), and higher than 0.5% assumed by Anderson and Brown (1993). No significant variation is observed between volcanoes. Hawaiian shrinkage bubbles tend to be larger than those from Iceland (Hartley et al., 2014; Neave et al., 2014) and the Azores (Métrich et al., 2014), which typically have $\phi \sim 1$ –2.5%. The distribution of Hawaiian

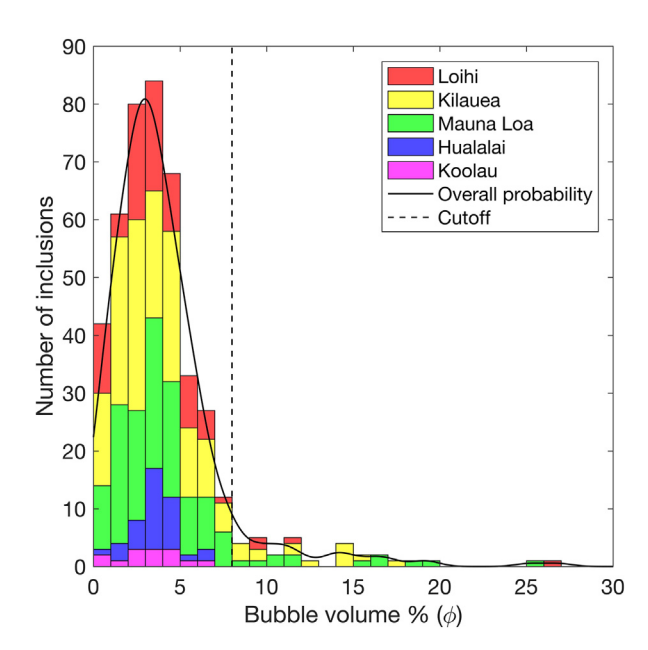


Fig. 6. Distribution of bubble volumes relative to melt inclusion volumes (ϕ) in melt inclusions from individual volcanoes (colored histograms). The black curve is the probability distribution of ϕ from all 437 Hawaiian melt inclusions. The overall distribution peaks strongly with a median of 3.3%, and no significant variation is observed between volcanoes. The long tail at higher values could represent trapped magmatic bubbles or fractured host olivine crystals, rather than shrinkage bubbles (e.g. Fig. 2f). Therefore, 30 melt inclusions with relative bubble volumes greater than 8% (dashed line) are excluded from our analyses.

bubble volume fractions contains some anomalous outliers with $\phi > \sim 8\%$, corresponding to extremely large bubbles (e.g. Fig. 2f). These outliers might not be shrinkage bubbles formed from the melt inclusion, but rather could be trapped magmatic bubbles, or indicate that host olivine crystals have fractured (Lowenstern, 1995). Consequently, the anomalously large bubbles with $\phi > 8\%$ are ignored. This cutoff eliminates 30 of the 437 analyzed samples. However, we note that the 8% cutoff is purely empirical based on the observed distribution (Fig. 6), and no robust method exists to distinguish trapped magmatic versus shrinkage bubbles.

3.2. Total CO₂ concentrations and the importance of shrinkage bubbles

The importance of shrinkage bubbles can be demonstrated by comparing dissolved CO₂ concentrations with the extent of post-entrapment crystallization correction in each inclusion (Fig. 7). As observed for Kilauea Iki inclusions (Sides et al., 2014a), the negative correlations in Fig. 7 indicate that significant quantities of CO₂ have been exsolved into bubbles due, at least in part, to post-entrapment crystallization.

Total (bubble + dissolved) CO_2 concentrations from the 407 Hawaiian melt inclusions vary by \sim 2 orders of magnitude, following approximately lognormal distribution, with maximum values in excess of 8000 ppm (Fig. 8, Tables 1, S1). Large variability exists both within and between volcanoes (Fig. 8), for example, Mauna Loa melt inclusions have relatively low CO_2 concentrations (median = 410 ppm; maximum = 4200 ppm), Kilauea intermediate (median = 890 ppm; maximum = 4900 ppm), and Loihi the highest (median = 1700 ppm; maximum = 8500 ppm).

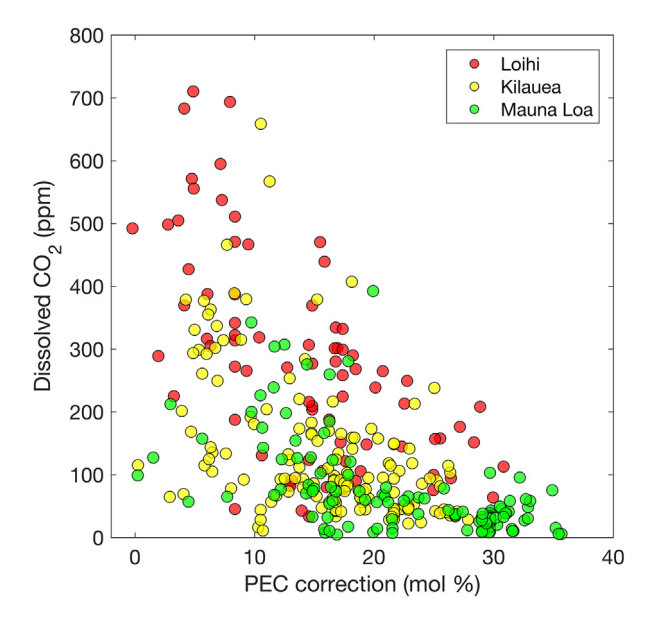


Fig. 7. Extent of post-entrapment crystallization (PEC) vs. measured dissolved CO_2 concentrations of Loihi, Mauna Loa, and Kilauea melt inclusions. The negative correlations indicate that CO_2 has exsolved to a shrinkage bubble during or associated with PEC (Sides et al., 2014a).

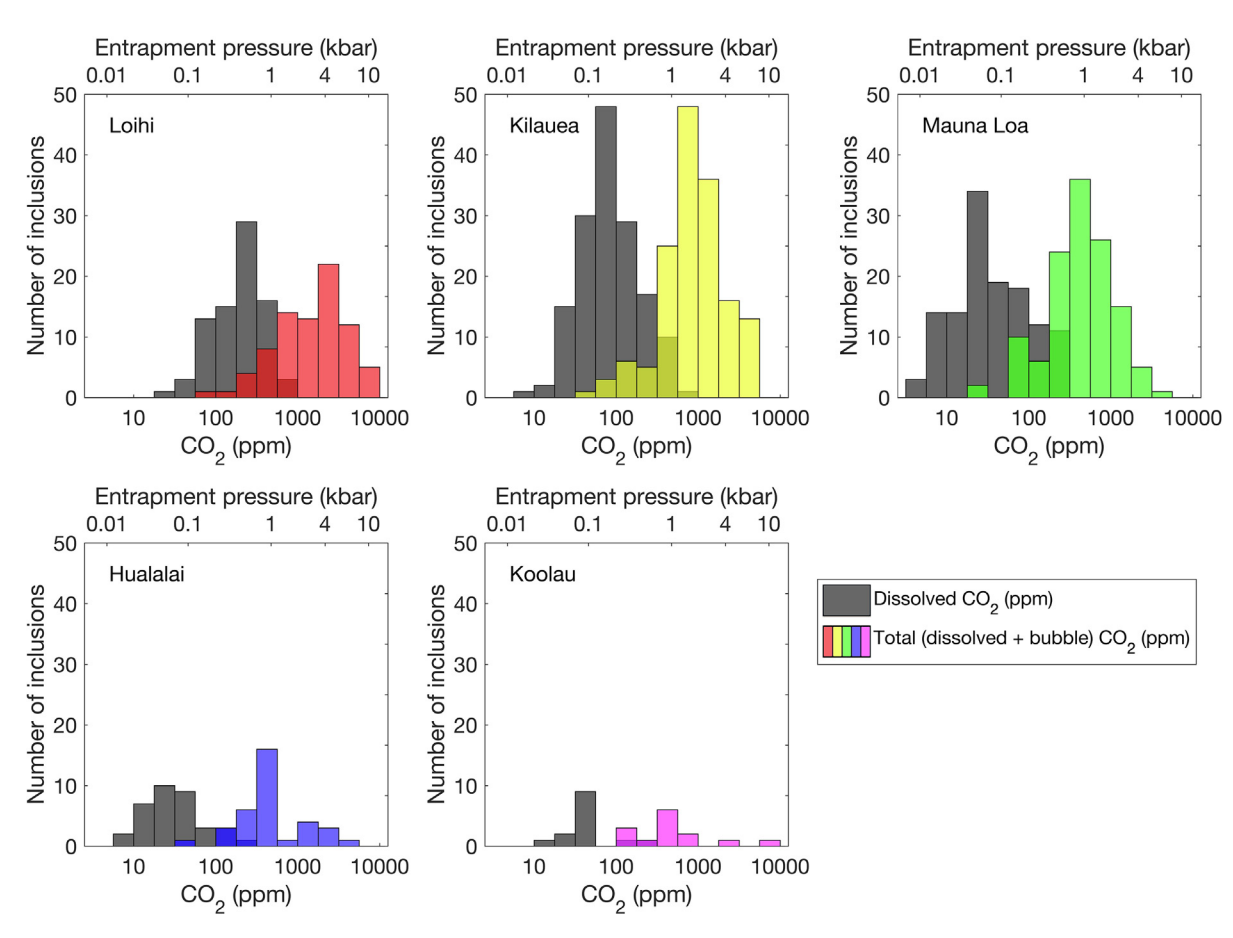


Fig. 8. Histograms of dissolved (grey) and total (dissolved + bubble; colored) CO_2 concentrations in olivine-hosted melt inclusions from five Hawaiian volcanoes. Total concentrations are often $\sim 10 \times$ higher than dissolved concentrations. The upper axis is the entrapment pressure corresponding to a given CO_2 concentration (Dixon et al., 1995).

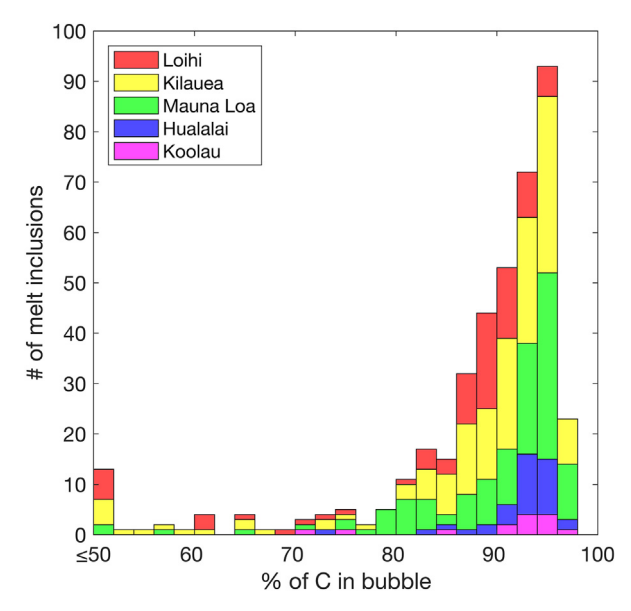


Fig. 9. Histogram of the proportion of C in the shrinkage bubble compared to the total C. More than 90% of the total C is sequestered in a shrinkage bubble in the majority of melt inclusions. This demonstrates the critical importance of accounting for shrinkage bubbles in measuring melt inclusion $\rm CO_2$ concentrations.

Shrinkage bubbles are inferred to contain the vast majority of the $\rm CO_2$ budget (Fig. 9) in the Hawaiian melt inclusions. In half of all melt inclusions, the shrinkage bubble contains at least 90% of the total $\rm CO_2$. On average, bubbles contain nearly $10\times$ the $\rm CO_2$ content of the glass. The finding that the vast majority of inclusion $\rm CO_2$ has been exsolved to a shrinkage bubble agrees with other studies of Hawaiian melt inclusions (Moore et al., 2015; Wallace et al., 2015; Tuohy et al., 2016). Consequently, accounting for $\rm CO_2$ exsolved to bubbles is critical for quantifying total $\rm CO_2$ concentrations in these melt inclusions.

3.3. CO₂-trace element ratios and the degassed nature of the samples

Mantle ratios of CO₂ to highly incompatible lithophile elements are tools to understand the long-term geologic behavior of C (Hauri et al., 2018; Hirschmann, 2018). Whereas CO₂ behaves like a highly incompatible element during partial melting and crystallization (Saal et al., 2002; Rosenthal et al., 2015), CO₂/X ratios (where X = Nb, Th, Ba, Rb) can significantly fractionate during magmatic degassing, complicating determination of mantle CO₂/X ratios. Because CO₂/X ratios are not affected by crystal fractionation (including post-entrapment crystalliza-

tion), sample suites with constant CO₂/X ratios have been interpreted to have experienced no degassing, and thus their CO₂/X ratios are representative of mantle source ratios (Saal et al., 2002; Michael and Graham, 2015; Shimizu et al., 2016; Le Voyer et al., 2017; Hauri et al., 2018).

The Hawaiian melt inclusions show a high degree of CO₂/Ba variability (Fig. 10), indicating that most samples have likely experienced degassing prior to entrapment. Consequently, the best estimate of pre-degassing or mantle ratios is the maximum CO₂/X ratio (e.g. Matthews et al., 2017). We randomly resampled each melt inclusion CO₂/ X ratio 10⁵ times from normal distributions based on their 1σ uncertainties to statistically estimate the maximum CO₂/ X ratio from each volcano (rather than simply choose the single maximum measured value). The average and standard deviation of the maximum values from each trial represent our estimate of the maximum CO₂/X ratio and its uncertainty, which are presented in Table 1 and shown as dashed lines in Fig. 10. The advantage of this Monte Carlo approach over using the maximum measured CO2/X ratio and its uncertainty is that it incorporates more data than just a single value, as there are often multiple individual measurements within uncertainty of the maximum measured value. Consequently, this approach provides a better estimate and lower uncertainty of the population maximum.

Inferred maximum CO_2/X ratios are highly variable between volcanoes (Table 1). For example, maximum CO_2/Ba ratios around 80-85 from Loihi, Hualalai, and Kilauea are similar to CO_2/Ba ratios of undegassed MORBs (75–100; Michael and Graham, 2015; Shimizu et al., 2016; Le Voyer et al., 2017) and Hawaiian North Arch lavas (80–115; Michael and Graham, 2015), but higher than Borgarhraun (northern Iceland; \sim 50; Hauri et al., 2018). Assuming they represent pre-degassing values, the maximum CO_2/Ba ratios from Koolau and Mauna Loa of \sim 35–40 are lower than any other known mantle domain. The maximum values from Hualalai and Koolau are based on small numbers of melt inclusions, so they may not be as robustly estimated as those from Loihi, Kilauea, and Mauna Loa.

3.4. CO₂ concentrations of parental magmas

In addition to pre-entrapment degassing, the parental magmas of melt inclusions are commonly modified by crystal fractionation prior to entrapment. Parental Hawaiian melts are in equilibrium with Fo_{90.6} olivine (Sobolev et al., 2005), whereas host olivine compositions in our dataset average Fo₈₈, indicating some olivine fractionation prior to inclusion entrapment. Therefore, CO₂ concentrations were corrected to be in equilibrium with Fo_{90.6} olivine by

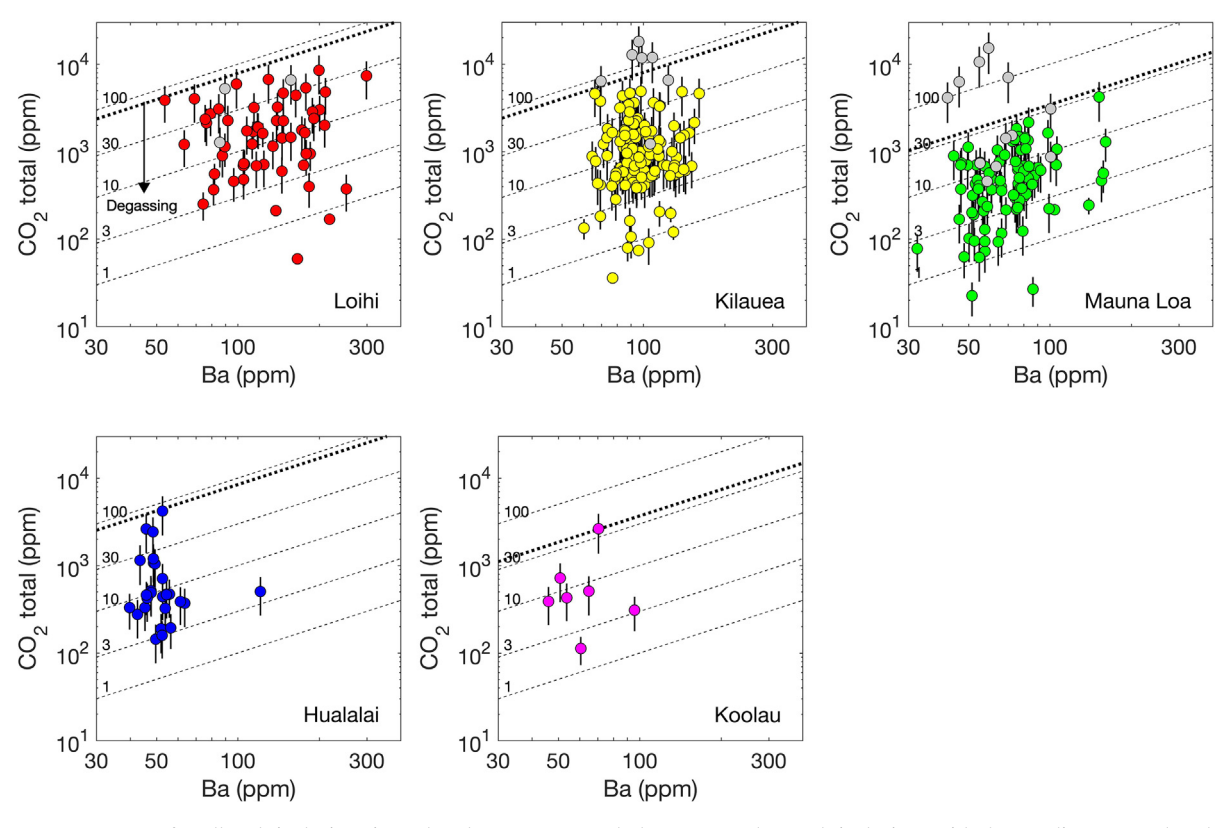


Fig. 10. CO_2 vs. Ba for all melt inclusions in each volcano. Grey symbols correspond to melt inclusions with ϕ exceeding 8%, and excluded from statistical analyses. Dashed lines indicate constant CO_2/Ba ratios. The highly variable CO_2/Ba ratios indicate that most magmas have likely experienced degassing prior to entrapment. Consequently, the maximum CO_2/Ba ratios observed (thick dashed lines; Table 1) represent minimum estimates of mantle source CO_2/Ba ratios.

Statistics on total (dissolved + bubble), parental, and mantle CO, concentrations, and maximum CO,/trace element ratios

	Loihi	Kilauea	Mauna Loa	Hualalai**	Koolau**
Number of MIs*	80	153	125	35	14
Mean CO ₂ (ppm)	2190	1230	590	720	1000
Median CO ₂ (ppm)	1750	890	410	430	500
Parental CO ₂ (ppm)	10330 ± 2300	6890 ± 1210	3860 ± 1250	4320 ± 1320	6040 ± 2450
Maximum CO ₂ /Ba	79 ± 18	80 ± 17	34 ± 6	84 ± 25	37 ± 15
Maximum CO ₂ /Nb	631 ± 169	594 ± 123	329 ± 80	627 ± 191	394 ± 166
Maximum CO ₂ /Rb	869 ± 183	1137 ± 248	539 ± 124	1066 ± 330	533 ± 223
Maximum CO_2/Th	11161 ± 3001	9503 ± 2084	4799 ± 894	10510 ± 3422	5432 ± 2279
F (%)	4.6	6.4	8.6	8.3	8.6
Mantle CO ₂ (ppm)	480 ± 110	440 ± 80	380 ± 120	360 ± 110	520 ± 210

Values are corrected for post-entrapment crystallization; parental concentrations are corrected to be in equilibrium with Fo-90.6 olivine (see text for details). Degree of melting (F) from Pietruszka et al. (2013) for Loihi, Kilauea, Mauna Loa and Koolau; from Norman and Garcia (1999) for Hualalai

* Excludes 30 melt inclusions with $\phi > 8\%$.

** Statistics are not well established due to small number of melt inclusions.

adding olivine to the melt compositions in 0.1% mass increments. This correction amounts to a dilution of the CO_2 concentration (16% on average; Table S1), which we assume behaves perfectly incompatibly.

Magmas are further modified from their parental compositions by degassing, and no samples are conclusively undegassed (Section 3.3). Consequently, we take maximum CO_2 concentrations corrected for pre-entrapment fractionation as estimates of parental CO_2 concentrations for each volcano. Parental CO_2 concentrations of each volcano were determined by resampling fractionation-corrected compositions 10^5 times from normal distributions defined by their 1σ uncertainty, similar to the method of determining maximum CO_2/X ratios (Section 3.3). Parental CO_2 concentrations range from 3900 ± 1300 ppm (Mauna Loa) to 6900 ± 1200 ppm (Kilauea) to $10,000 \pm 2000$ ppm (Loihi; Table 1).

Our estimate of $6900 \pm 1200 \,\mathrm{ppm}$ CO₂ in parental Kilauea magmas is similar to estimates of 7000-9600 based on calculated magma supply rates and CO2 emission measurements for recent activity (Gerlach et al., 2002; Anderson and Poland, 2017). However, our estimate of $10,000 \pm 2000$ ppm CO₂ in parental Loihi magmas is somewhat higher than the maximum CO₂ content of 6300 ppm obtained by combining measured dissolved and inferred vesicular CO₂ contents in Loihi basalt glasses (Dixon and Clague, 2001), although that estimate was based on only 19 samples, compared to 80 in this study (Table 1). Predegassing CO₂ concentrations in Loihi magmas, reconstructed from noble gas compositions and a disequilibrium degassing model, have been estimated to range up to ~6000 ppm (Gonnermann and Mukhopadhyay, 2007), although those results may be sensitive to the degassing model parameters used, such as the magmatic C diffusivity, which is not well constrained (Tucker et al., 2018). The CO₂ concentrations calculated here represent upper limits because nonequilibrium bubble expansion was assumed to be insignificant (Section 2.3.2). This assumption is supported by the agreement (within ~40%) between our estimate of the parental Kilauea CO2 concentration and estimates based on magma supply rates and CO₂ emissions.

4. COMPARISON TO OTHER METHODS FOR RECONSTRUCTING TOTAL CO₂ CONCENTRATIONS

Whereas the equation of state method calculates ρ_v in shrinkage bubbles, Raman spectroscopy provides a means to directly measure this quantity (e.g. Esposito et al., 2011; Hartley et al., 2014; Moore et al., 2015; Aster et al., 2016). Therefore, comparison of results obtained by both methods can be used to test the assumptions of the equation of state method. Such a comparison in 22 melt inclusions from Kilauea, Seguam, and Fuego found an average of $3\times$ lower CO₂ concentrations by Raman spectroscopy (Moore et al., 2015) compared to an equation of state method similar to ours. Similarly, Neave et al. (2014) and Bali et al. (2018) were unable to detect CO₂ vapor by Raman spectroscopy in Icelandic melt inclusion vapor bubbles despite large contributions to CO₂ inferred from an

equation of state method. These discrepancies were explained by nonequilibrium bubble expansion (Section 2.3.2), implying overestimates of CO₂ concentrations by an equation of state method.

Another possible explanation for the discrepancy between total CO₂ concentrations determined by the Raman and equation of state methods is the presence of C phases not detectable by Raman spectroscopy. For example, supercritical CO₂ fluid would separate into liquid and vapor during approach to ambient conditions, and the Raman spectroscopy method would fail to quantify any liquid CO₂ (Maclennan, 2017). Additionally, late-stage carbon precipitation onto bubble surfaces could occur without changing the bubble size. Indeed, Moore et al. (2015) also identified carbonate minerals in many melt inclusions. Unlike the Raman spectroscopy method, which is only quantitatively sensitive to vapor phase CO₂, the equation of state method is valid even if solid or liquid C phases are present.

Textures of precipitated solids are observed on nearly all bubble surfaces in this study (Fig. 2e, f, 11a), which are especially apparent using dark field illumination. Identical textures are observed whether or not bubbles have been exposed by polishing, indicating the texture is not a product of the polishing process. Energy-dispersive X-ray spectroscopy (EDS) analysis of textured surfaces reveals they are C-rich (Fig. 11b). Although small Fe-Cu-S grains are occasionally observed, C-bearing solids ubiquitously coat all bubble surfaces examined, indicating the presence of precipitated C phases, perhaps carbonates and/or amorphous C (e.g. Mathez and Delaney, 1981; Kamenetsky et al., 2002). C-bearing solids are capable of sequestering large amounts of C. For example, a 100 nm layer of amorphous C ($\rho = 2 \text{ g/cm}^3$) on a 20 µm radius bubble in a melt inclusion with $\phi = 3\%$ would sequester 1200 ppm CO₂. Therefore, C precipitation can sequester a large amount of the bubble's C, and decrease the bubble vapor density measured by Raman spectroscopy.

Another method to explicitly measure vapor bubble CO₂ is to heat the inclusion to re-dissolve (homogenize) the bubble into the melt (e.g. Hauri, 2002; Mironov et al., 2015; Wallace et al., 2015; Tuohy et al., 2016). Carbon phases, if present, should also re-dissolve into the melt, mitigating the problem of precipitated carbon phases. Comparisons between populations of homogenized and unhomogenized melt inclusions from Mauna Loa and Kilauea were performed by Wallace et al. (2015) and Tuohy et al. (2016), respectively. They found that homogenized melt inclusions generally had higher dissolved CO₂ concentrations than unhomogenized melt inclusions by factors of \sim 2–4, implying at least partial re-dissolution of shrinkage bubble C into the melt. Hauri (2002) also studied homogenized melt inclusions from Loihi, Kilauea, Mauna Loa, and Koolau, but did not make a comparison to unhomogenized inclusions. However, the homogenized samples from all three studies generally have significantly less CO2 than determinations using Raman spectroscopy or our equation of state method; for example, the average CO₂ concentration of Kilauea melt inclusions determined by homogenization is 260 ppm (n = 84; Hauri, 2002; Tuohy et al., 2016),

850 ppm by Raman spectroscopy (n = 55; Moore et al., 2015), and 1030 ppm by our equation of state methodology (n = 153; Table 1). Although some of this variation is undoubtedly due to the different samples studied, the lower values found by homogenization could indicate that homogenization did not fully dissolve all shrinkage bubble CO_2 , evidenced by the reappearance or non-disappearance of bubbles in some inclusions, and/or that CO_2 was lost during homogenization, possibly evidenced by the appearance of cracks in some samples.

Clearly, comparative studies on large numbers of melt inclusions from the same samples are needed to understand the discrepancies in total CO_2 concentrations determined by the equation of state, Raman spectroscopy, and homogenization methods. It should also be noted that the large (\sim 50%) uncertainty in the equation of state method is not mitigated by Raman spectroscopy, as it results from ϕ rather than ρ_v , but is mitigated by the homogenization method. Additionally, a Raman detection limit of ρ_v - \sim 0.04 g/cm³ (Hartley et al., 2014; Neave et al., 2014) represents a vapor CO_2 detection limit of a few hundred parts per million (depending on the bubble size), implying bubbles without detectable CO_2 by Raman spectroscopy could still house a significant fraction of a melt inclusion's C.

5. ORIGIN OF INTER-VOLCANO CO2 VARIABILITY

A distinctive trend of decreasing CO₂ concentrations is observed from the southeast toward the northwest: Loihi has the highest CO₂ concentration, Kilauea intermediate, and Mauna Loa the lowest (Table 1). Hauri (2002) also noted that melt inclusions from Loihi tended to have higher CO₂ than those from other Hawaiian volcanoes. The inactive volcanoes Hualalai and Koolau may also have intermediate CO₂, although they are not well constrained due to the small number of samples. Three possible explanations for these variations are explored below: differences in magma chamber pressure, differences in the degree of melting, and differences in the mantle source CO₂ concentration. We emphasize that these possible explanations are not mutually exclusive.

5.1. Magma chamber pressure

CO₂ concentrations of melt inclusions are potentially sensitive indicators of equilibrium degassing pressures, as magmatic CO₂ solubility is a strong function of pressure (e.g. Mysen et al., 1976; Pan et al., 1991). Because the melt inclusions primarily derive from degassed magmas (Fig. 10), their CO₂ concentrations can be interpreted as entrapment pressures. These pressures would be inferred to increase from Mauna Loa to Kilauea to Loihi—the CO₂ concentrations imply median entrapment pressures ranging from 1.0 kbar (Mauna Loa), 1.8 kbar (Kilauea), to 3.3 kbar (Loihi), indicating that the majority of inclusions record upper- to mid-crustal entrapment depths; the Hawaiian Moho is at ~4.5–6 kbar (13–18 km depth; Hill and Zucca, 1987). Maximum entrapment pressures of 6.3 kbar (Mauna Loa), 9.7 kbar (Kilauea) and 12.4 kbar

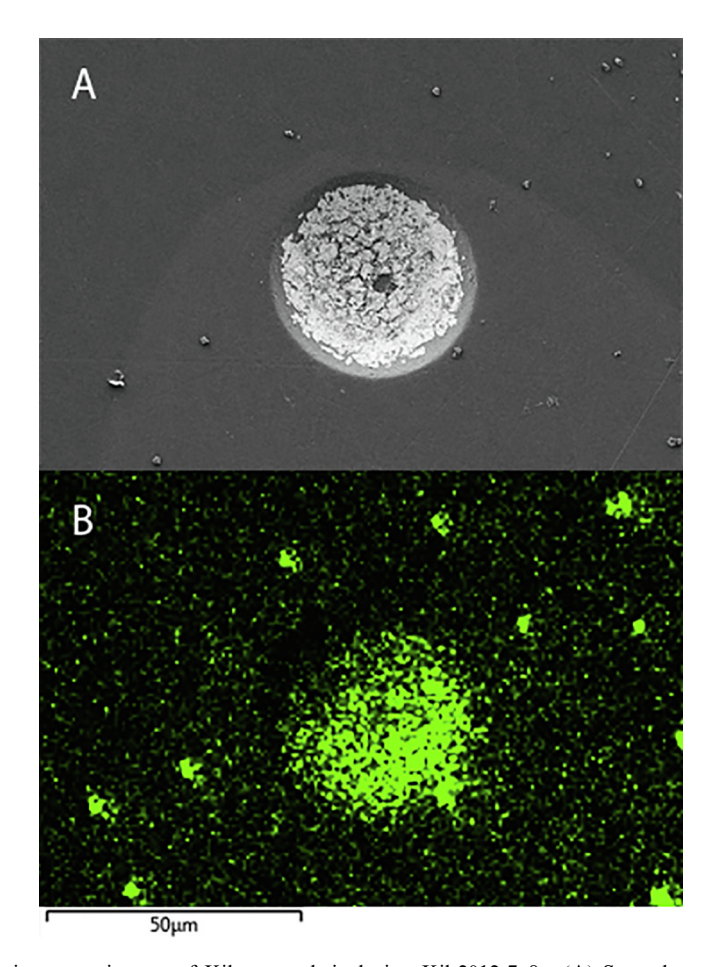


Fig. 11. Secondary electron microscope images of Kilauea melt inclusion Kil-2012-7_8a. (A) Secondary electron image showing that the bubble has been mostly polished away and the remaining surface is relatively flat. The interior of the bubble is characterized by a rough texture, which appears to have been polished away near the edges. The outline of the melt inclusion is visible as a subtle change in brightness. (B) Carbon map reveals that the surface of the bubble is very C-rich, indicating a precipitated solid carbon phase. Some shadowing reduces C intensity in the upper-left section of the bubble. Carbon hotspots away from the bubble spatially correlate with 1-μm diamond grains left over from polishing.

(Loihi) indicate that a small amount of olivine crystallization and melt inclusion entrapment may occur at lower crustal to uppermost mantle pressures.

There is some correspondence between CO₂ concentrations and magma chamber depths among the active volcanoes. The main magma chamber for Loihi's 1996 eruption was inferred to be located 8-9 km below sea level (Garcia et al., 2006), corresponding to \sim 2.2 kbar, whereas the magma under Mauna Loa is in the range of 3-5 km below the volcanic summit (Poland et al., 2014), corresponding to 0.8-1.4 kbar. Consequently, CO₂ would be more extensively degassed in Mauna Loa's shallower magma chamber, leading to lower CO2 concentrations in Mauna Loa melt inclusions than in Loihi melt inclusions. However, Kilauea melt inclusions have $\sim 2 \times$ higher CO₂ concentrations than those from Mauna Loa (Table 1), yet their magma chambers are at approximately the same depth beneath the volcanic summit (Poland et al., 2014). Therefore, while degassing processes are clearly important in establishing the variability in CO2 concentrations within individual volcanoes (Fig. 10, Section 3.3), the depth of the main magma chamber alone cannot account for the higher median and maximum CO_2 concentrations in Kilauea compared to Mauna Loa.

5.2. Degree of melting

Variations in parental CO_2 concentrations between volcanoes could be due to differences in the degree of melting (F) of their mantle source. Explaining the variability of parental CO_2 solely by varying F requires the lowest F at Loihi, intermediate at Kilauea, and highest at Mauna Loa, broadly similar to the relative pattern needed to explain trace elements (Norman and Garcia, 1999; Pietruszka et al., 2013). Assuming F = 4.6% at Loihi, 6.4% at Kilauea, and 9.8% at Mauna Loa (Pietruszka et al., 2013), mantle CO_2 concentrations are approximately 480 ppm at Loihi, 440 ppm at Kilauea, and 380 ppm at Mauna Loa.

While these inferred mantle source CO_2 concentrations have a smaller relative variation (25%) than parental magma CO_2 concentrations (factor of \sim 2.7), it is unlikely that the Hawaiian mantle has a uniform CO_2 concentra-

tion. Ratios of CO_2 to highly incompatible lithophile elements such as Ba vary by more than a factor of \sim 2 between Kilauea and Mauna Loa (Table 1). Such variability cannot be caused by $F > \sim 1\%$, suggesting possible heterogeneity in source CO_2 /Ba ratios. The similar factor of \sim 2 lower parental magma CO_2 concentration at Mauna Loa (compared to Kilauea) suggests that the difference in CO_2 /Ba is due to CO_2 , rather than Ba. This agrees with geochemical models that show limited variation in ratios of highly incompatible trace element concentrations between different Hawaiian shield volcanoes (Norman and Garcia, 1999; Pietruszka et al., 2013).

5.3. Source heterogeneity

Variations in the degree of melting and depth of degassing can account for some, but likely not all, of the variation in CO_2 concentrations between the different volcanoes. Thus, some source heterogeneity is probably required; specifically, mantle CO_2 concentration might decrease towards the northwest, such that Loihi has the highest mantle CO_2 concentration (\sim 480 ppm), Kilauea is intermediate (\sim 440 ppm), Mauna Loa the lowest (\sim 380 ppm).

If C is subducted in association with oceanic crust, this trend could reflect the amount of recycled crust in the mantle source of the volcanoes. However, estimates of the relative amount of recycled crust are opposite to the observed trend in CO₂ concentrations: Mauna Loa has been estimated to have the highest amount of recycled material, Kilauea intermediate, and Loihi the lowest (Hauri, 1996; Sobolev et al., 2005; Pietruszka et al., 2013). Additionally, there is no obvious association between C and the Loa-Kea spatial or isotopic dichotomy (e.g., Abouchami et al., 2005; Weis et al., 2011); Loihi and Mauna Loa are both Loa-type volcanoes but have the highest and lowest CO₂ concentrations, respectively.

An alternative explanation for the northwestern spatial decrease of source C is progressive depletion of the Hawaiian plume source. Under this hypothesis, Loihi samples the most pristine plume material, which becomes more depleted downstream. Such a model has been used to explain the He isotopic distribution in the Hawaiian volcanoes, where He is transported via low-degree volatile-rich or carbonatitic incipient melts, preferentially sampled at the leading edge of the plume (Loihi), and the older volcanoes increasingly sample a more depleted source approaching the ambient mantle (Kurz et al., 1995; Valbracht et al., 1996; Hanyu et al., 2005; Dixon et al., 2008; Hofmann et al., 2011). This model can additionally explain why Loihi has the highest CO₂ concentration despite the lowest amount of recycled crust.

6. CARBON ENRICHMENT IN THE HAWAIIAN MANTLE

The results presented here suggest that the Hawaiian mantle is significantly more C-rich than the MORB mantle. Whereas the active Hawaiian volcanoes have mantle source CO₂ concentrations ranging from 380 to 480 ppm (Sec-

tion 5.2, Table 1), the MORB mantle has approximately 60–140 ppm CO₂ (Saal et al., 2002; Hirschmann and Dasgupta, 2009; Michael and Graham, 2015; Rosenthal et al., 2015; Le Voyer et al., 2017; Tucker et al., 2018). The factor of 3–8× enrichment of CO₂ in the Hawaiian mantle compared to the MORB mantle could be due to enhanced subduction of C to the Hawaiian mantle, the presence of C-rich primitive material in the Hawaiian mantle, or both.

If surficial C is subducted in association with recycled crust, the higher C concentration in the Hawaiian mantle could reflect preferential delivery of subducted C to the deep mantle source of Hawaii, compared to the shallower MORB mantle. This scenario is consistent with geodynamic and mass balance arguments for predominantly surfacederived mantle C (Javoy et al., 1982; Trull et al., 1993; Zhang and Zindler, 1993; Hirschmann, 2018) and the inference that the Hawaiian mantle contains significant amounts of subducted material (e.g. Lassiter and Hauri, 1998; Sobolev et al., 2005; Pietruszka et al., 2013). While the form of this subducted C is speculative, up to a few percent carbonates have been implicated to explain Hawaiian Ca and Sr isotopic compositions (Huang et al., 2011). Only 1% CaCO₃ would provide ~4400 ppm CO₂, implying that subducting crust could be extensively (>90%) decarbonated but still deliver sufficient C to the Hawaiian mantle to explain its CO₂ concentration, and Ca and Sr isotopic compositions. Even though the amount of recycled crust may not explain the inter-volcano C variability (Section 5.2), recycled material may still be an important source of C to the Hawaiian plume.

On the other hand, the possibility of primitive material in the Hawaiian mantle is supported by the enrichment in primordial noble gases in Hawaiian basalts compared to mid-ocean ridge basalts (e.g. Craig and Lupton, 1976; Kurz et al., 1982; Honda et al., 1991). The mantle source of Loihi (480 ppm CO₂) could comprise 13% primitive material with 3000 ppm CO₂ (similar to the highest estimates of the bulk silicate Earth CO₂ concentration; Marty, 2012) and 87% MORB-like depleted mantle with 100 ppm CO₂. Although the amount of primitive material needed to enrich the Hawaiian mantle strongly depends on the poorly constrained primitive mantle CO₂ concentration, 10% to a few tens of percent primitive material is permitted by trace element modeling of Hawaiian magma compositions (Pietruszka et al., 2013).

The higher CO_2 concentrations in the mantle sources of OIBs compared to MORBs suggest they disproportionately contribute to global CO_2 fluxes from the mantle. Assuming a parental CO_2 concentration of 7000 ± 1900 ppm (the average and standard error of the Loihi, Kilauea, and Mauna Loa parental compositions) and a Hawaiian magmatic flux of 0.20 ± 0.08 km³/year (Poland et al., 2014), the Hawaiian CO_2 flux is $3.8 \pm 1.8 \times 10^{12}$ g/year. This flux corresponds to 6% of the mid-ocean ridge flux of 5.9×10^{13} g/year (Tucker et al., 2018), despite constituting only 1% the magmatic flux. However, the Hawaiian CO_2 flux is still around $10,000 \times$ lower than anthropogenic CO_2 emissions of $\sim 4 \times 10^{16}$ g/year (Le Quéré et al., 2018).

7. CONCLUSIONS

 CO_2 concentrations were measured in 437 melt inclusions from Loihi, Kilauea, Mauna Loa, Hualalai, and Koolau with the goal of understanding the role of plumes in the global carbon cycle. Shrinkage bubble CO_2 contents were calculated from their relative volumes and an equation of state, and added to dissolved CO_2 contents. Thirty melt inclusions had unusually large bubbles, which may be trapped magmatic bubbles rather than shrinkage bubbles.

The uncertainty associated with the relative volume measurements can be quite large, up to ${\sim}50\%~(1\sigma)$, when melt inclusion volume is determined from a 2-dimensional polished section. This uncertainty is applicable regardless of whether CO_2 vapor density is calculated from an equation of state or measured by Raman spectroscopy. Therefore, a large number of inclusions must be analyzed to robustly estimate the statistics of a dataset. Additionally, the equation of state methodology does not account for the possibility of nonequilibrium bubble expansion, and more work is required to clarify the conditions under which this might occur.

Typically, $\sim 90\%$ of melt inclusion CO_2 has been exsolved to a shrinkage bubble, indicating that accurate accounting for exsolved CO_2 is required to study total CO_2 concentrations. In the Hawaiian melt inclusions, much of this CO_2 has likely been precipitated as solid carbon phases on the bubble walls, and thus would not be accounted for by Raman spectroscopy.

Total (dissolved + bubble) CO_2 concentrations predominantly imply upper- to mid-crustal entrapments pressures, with some small amount of crystallization and entrapment occurring in the lower crust uppermost mantle. Parental Hawaiian magmas from the active Mauna Loa, Kilauea, and Loihi volcanoes range from 3900 to 10,000 ppm CO_2 , with an average of 7000 ± 1900 ppm, corresponding to a Hawaiian CO_2 flux of 3.8 ± 1.8 Tg/year. The variation in parental CO_2 concentrations between the volcanoes can be explained by a model of progressive depletion of the Hawaiian mantle source towards the northwest, although differences in magma chamber depth may also play a role.

Mantle source CO₂ concentrations of the active Hawaiian volcanoes range from 380 to 480 ppm, significantly more CO₂-rich than the MORB mantle. This enrichment likely results from enhanced subduction of surficial C to the mantle source of the Hawaiian plume and/or the presence of C-rich primitive material in the Hawaiian plume.

ACKNOWLEDGEMENTS

We are indebted to Jim Kauahikaua, David Okita, and the Hawaiian Volcano Observatory for helicopter support during sampling of Mauna Loa cinder cones; Jianhua Wang for assistance in the Carnegie SIMS lab; Anaïs Bardyn and Emma Bullock for assistance with SEM analyses; and Larry Nittler for assistance with photomicrography. This paper benefited from thorough reviews by Jake Lowenstern, Dave Graham, John Maclennan, and an anonymous reviewer, as well as discussions with Kei Shimizu and Megan Newcombe. This work was supported by Deep Carbon Observatory postdoctoral fellowships to J.M.T. and J.P.M. This paper is SOEST contribution #10675 and is a contribution to the

Deep Carbon Observatory. Any use of trade, firm, or product names is for descriptive purposes only and does not imply endorsement by the U.S. Government.

APPENDIX A. SUPPLEMENTARY MATERIAL

Supplementary data to this article can be found online at https://doi.org/10.1016/j.gca.2019.04.001.

REFERENCES

- Abouchami W., Hofmann A. W., Galer S. J. G., Frey F., Eisele J. and Feigenson M. (2005) Lead isotopes reveal bilateral asymmetry and vertical continuity in the Hawaiian mantle plume. *Nature* **434**, 851–856.
- Anderson A. T. and Brown G. G. (1993) CO₂ contents and formation pressures of some Kilauean melt inclusions. Am. Mineral. 78, 794–803.
- Anderson K. R. and Poland M. P. (2017) Abundant carbon in the mantle beneath Hawa'i. *Nat. Geosci.* **10**, 704–708.
- Aster E. M., Wallace P. J., Moore L. R., Watkins J., Gazel E. and Bodnar R. J. (2016) Reconstructing CO₂ concentrations in basaltic melt inclusions using Raman analysis of vapor bubbles. J. Volcanol. Geoth. Res. 323, 148–162.
- Bali E., Hartley M. E., Halldórsson S. A., Gudfinnsson G. H. and Jakobsson S. (2018) Melt inclusion constraints on volatile systematics and degassing history of the 2014–2015 Holuhraun eruption, Iceland. *Contrib. Mineral. Petrol.* 173, 9.
- Craig H. and Lupton J. E. (1976) Primordial neon, helium, and hydrogen in oceanic basalts. *Earth Planet. Sci. Lett.* 31, 369– 385.
- Dasgupta R. and Hirschmann M. M. (2010) The deep carbon cycle and melting in Earth's interior. *Earth Planet. Sci. Lett.* 298, 1– 13.
- Dixon J. E., Stolper E. M. and Holloway J. R. (1995) An experimental study of water and carbon dioxide solubilities in mid-ocean ridge basaltic liquids. Part I: calibration and solubility models. J. Petrol. 36, 1607–1631.
- Dixon J., Clague D. A., Cousens B., Monsalve M. L. and Uhl J. (2008) Carbonatite and silicate melt metasomatism of the mantle surrounding the Hawaiian plume: Evidence from volatiles, trace elements, and radiogenic isotopes in rejuvenated-stage lavas from Niihau, Hawaii. Geochem. Geophys. Geosys. 9, Q09005.
- Dixon J. E. and Clague D. A. (2001) Volatiles in basaltic glasses from Loihi Seamount, Hawaii: Evidence for a relatively dry plume component. J. Petrol. 42, 627–654.
- Dodson M. H. (1973) Closure temperature in cooling geochronological and petrological systems. *Contrib. Mineral. Petrol.* 40, 259–274.
- Duan Z. and Zhang Z. (2006) Equation of state of the H₂O, CO₂, and H₂O–CO₂ systems up to 10 GPa and 2573.15 K: Molecular dynamics simulations with ab initio potential surface. *Geochim. Cosmochim. Acta* **70**, 2311–2324.
- Edmonds M., Sides I. R., Swanson D. A., Werner C., Martin R. S., Mather T. A., Herd R. A., Jones R. L., Mead M. I., Sawyer G. and Roberts T. J. (2013) Magma storage, transport and degassing during the 2008–10 summit eruption at Kīlauea Volcano, Hawai'i. Geochim. Cosmochim. Acta 123, 284–301.
- Esposito R., Bodnar R. J., Danyushevsky L. V., De Vivo B., Fedele L., Hunter J., Lima A. and Shimizu N. (2011) Volatile evolution of magma associated with the Solchiaro eruption in the Phlegrean Volcanic District (Italy). *J. Petrol.* **52**, 2431–2460.

- French S. W. and Romanowicz B. (2015) Broad plumes rooted at the base of the Earth's mantle beneath major hotspots. *Nature* **525**, 95–99.
- Garcia M. O., Caplan-Auerbach J., Eric H., Kurz M. D. and Becker N. (2006) Geology, geochemistry and earthquake history of Löihi Seamount, Hawaii's youngest volcano. *Chem. Erde Geochem.* 66, 81–108.
- Gerlach T. M., McGee K. A., Elias T., Sutton A. J. and Doukas M. P. (2002) Carbon dioxide emission rate of Kīlauea Volcano: Implications for primary magma and the summit reservoir. J. Geophys. Res. 107, 2189.
- Gonnermann H. M. and Mukhopadhyay S. (2007) Nonequilibrium degassing and a primordial source for helium in ocean-island volcanism. *Nature* **449**, 1037–1040.
- Guillot B. and Sator N. (2011) Carbon dioxide in silicate melts: A molecular dynamics simulation study. *Geochim. Cosmochim.* Acta 75, 1829–1857.
- Hanyu T., Clague D. A., Kaneoka I., Dunai T. J. and Davies G. R. (2005) Noble gas systematics of submarine alkalic lavas near the Hawaiian hotspot. *Chem. Geol.* 214, 135–155.
- Hartley M. E., Maclennan J., Edmonds M. and Thordarson T. (2014) Reconstructing the deep CO₂ degassing behaviour of large basaltic fissure eruptions. *Earth Planet. Sci. Lett.* 393, 120–131.
- Hauri E. H. (1996) Major-element variability in the Hawaiian mantle plume. *Nature* **382**, 415–419.
- Hauri E. (2002) SIMS analysis of volatiles in silicate glasses, 2: isotopes and abundances in Hawaiian melt inclusions. *Chem. Geol.* 183, 115–141.
- Hauri E. H., Maclennan J., McKenzie D., Gronvold K., Oskarsson N. and Shimizu N. (2018) CO₂ content beneath northern Iceland and the variability of mantle carbon. *Geology* 46, 55–58.
- Hill D. P. and Zucca J. J. (1987) Geophysical constraints on the structure of Kilauea and Mauna Loa volcanoes and some implications for seismomagmatic processes. US Geol. Surv. Prof. Pap. 1350, 903–917.
- Hirschmann M. M. and Dasgupta R. (2009) The H/C ratios of Earth's near-surface and deep reservoirs, and consequences for deep Earth volatile cycles. *Chem. Geol.* 262, 4–16.
- Hirschmann M. M. (2018) Comparative deep Earth volatile cycles: The case for C recycling from exosphere/mantle fractionation of major (H₂O, C, N) volatiles and from H₂O/Ce, CO₂/Ba, and CO₂/Nb exosphere ratios. *Earth Planet. Sci. Lett.* **502**, 262–273.
- Hofmann A. W., Farnetani C. G., Spiegelman M. and Class C. (2011) Displaced helium and carbon in the Hawaiian plume. *Earth Planet. Sci. Lett.* **312**, 226–236.
- Honda M., McDougall I., Patterson D. B., Doulgeris A. and Clague D. A. (1991) Possible solar noble-gas component in Hawaiian basalts. *Nature* **349**, 149–151.
- Huang S., Farkaš J. and Jacobsen S. B. (2011) Stable calcium isotopic compositions of Hawaiian shield lavas: evidence for recycling of ancient marine carbonates into the mantle. *Geochim. Cosmochim. Acta* 75, 4987–4997.
- Iacono-Marziano G., Morizet Y., Le Trong E. and Gaillard F. (2012) New experimental and semi-empirical parameterization of H2O-CO2 solubility in mafic melts. *Geochim. Cosmochim.* Acta 97, 1–23.
- Javoy M., Pineau F. and Allègre C. J. (1982) Carbon geodynamic cycle. *Nature* 300, 171–173.
- Kamenetsky V. S., Davidson P., Mernagh T. P., Crawford A. J., Gemmell J. B., Portnyagin M. V. and Shinjo R. (2002) Fluid bubbles in melt inclusions and pillow-rim glasses: high-temperature precursors to hydrothermal fluids? *Chem. Geol.* 183, 349–364.
- Kelemen P. B. and Manning C. E. (2015) Reevaluating carbon fluxes in subduction zones, what goes down, mostly comes up. *Proc. Natl. Acad. Sci.* 112, E3997–E4006.

- Kurz M. D., Jenkins W. J. and Hart S. R. (1982) Helium isotopic systematics of oceanic islands and mantle heterogeneity. *Nature* 297, 43–47.
- Kurz M. D., Kenna T. C., Kammer D. P., Rhodes J. M. and Garcia M. O. (1995) Isotopic evolution of Mauna Loa Volcano: A view from the submarine southwest rift zone. AGU Monograph Ser. 92, 289–306.
- Lassiter J. C. and Hauri E. H. (1998) Osmium-isotope variations in Hawaiian lavas: evidence for recycled oceanic lithosphere in the Hawaiian plume. *Earth Planet. Sci. Lett.* 164, 483–496.
- Le Quéré C., Andrew R. M., Friedlingstein P., Sitch S., Pongratz J., Manning A. C., Korsbakken J. I., Peters G. P., Canadell J. G., Jackson R. B., Boden T. A., Tans P. P., Andrews O. D., Arora V. K., Bakker D. C. E., Barbero L., Becker M., Betts R. A., Bopp L., Chevallier F., Chini L. P., Ciais P., Cosca C. E., Cross J., Currie K., Gasser T., Harris I., Hauck J., Haverd V., Houghton R. A., Hunt C. W., Hurtt G., Ilyina T., Jain A. K., Kato E., Kautz M., Keeling R. F., Klein Goldewijk K., Körtzinger A., Landschützer P., Lefèvre N., Lenton A., Lienert S., Lima I., Lombardozzi D., Metzl N., Millero F., Monteiro P. M. S., Munro D. R., Nabel J. E. M. S., Nakaoka S., Nojiri Y., Padin X. A., Peregon A., Pfeil B., Pierrot D., Poulter B., Rehder G., Reimer J., Rödenbeck C., Schwinger J., Séférian R., Skjelvan I., Stocker B. D., Tian H., Tilbrook B., Tubiello F. N., van der Laan-Luijkx I. T., van der Werf G. R., van Heuven S., Viovy N., Vuichard N., Walker A. P., Watson A. J., Wiltshire A. J., Zaehle S. and Zhu D. (2018) Global Carbon Budget 2017. Earth Sys. Sci. Data 10, 405-448.
- Le Voyer M., Kelley K. A., Cottrell E. and Hauri E. H. (2017) Heterogeneity in mantle carbon content from CO₂-undersaturated basalts. *Nature Comm.* **8**, 14062.
- Le Voyer M., Hauri E. H., Cottrell E., Kelley K. A., Salters V. J. M., Langmuir C. H., Hilton D. R., Barry P. H. and Füri E. (2019) Carbon fluxes and primary magma CO₂ contents along the global mid-ocean ridge system. *Geochem. Geophys. Geosys.* 20. GC007630.
- Lowenstern J. B. (1995) Applications of silicate-melt inclusions to the study of magmatic volatiles. In *Magmas, fluids, and ore* deposits. Mineralogical Association of Canada, pp. 71–99.
- Maclennan J. (2017) Bubble formation and decrepitation control the CO₂ content of olivine-hosted melt inclusions. *Geochem. Geophys. Geosys.* **18**, GC006633.
- Marske J. P. and Hauri E. H. (2019) Major- and trace-element compositions of 915 melt inclusions and host olivines from Hawaiian shield volcanoes. *Interdisciplinary Earth Data Alli*ance (IEDA). https://doi.org/10.1594/IEDA/111193.
- Marty B. (2012) The origins and concentrations of water, carbon, nitrogen and noble gases on Earth. *Earth Planet. Sci. Lett.* **313–314**, 56–66.
- Mason E., Edmonds M. and Turchyn A. V. (2017) Remobilization of crustal carbon may dominate volcanic arc emissions. *Science* **357**, 290–294.
- Mathez E. A. and Delaney J. R. (1981) The nature and distribution of carbon in submarine basalts and peridotite nodules. *Earth Planet. Sci. Lett.* **56**, 217–232.
- Matthews S., Shorttle O., Rudge J. F. and Maclennan J. (2017) Constraining mantle carbon: CO₂-trace element systematics in basalts and the roles of magma mixing and degassing. *Earth Planet. Sci. Lett.* **480**, 1–14.
- Métrich N., Zanon V., Créon L., Hildenbrand A., Moreira M. and Marques F. O. (2014) Is the 'Azores hotspot' a wetspot? Insights from the geochemistry of fluid and melt inclusions in olivine of Pico basalts. J. Petrol. 55, 377–393.
- Michael P. J. and Graham D. W. (2015) The behavior and concentration of CO₂ in the suboceanic mantle: inferences from

- undegassed ocean ridge and ocean island basalts. *Lithos* 236, 338–351
- Mironov N., Portnyagin M., Botcharnikov R., Gurenko A., Hoernle K. and Holtz F. (2015) Quantification of the CO₂ budget and H₂O-CO₂ systematics in subduction-zone magmas through the experimental hydration of melt inclusions in olivine at high H₂O pressure. *Earth Planet. Sci. Lett.* **425**, 1–11.
- Montelli R., Nolet G., Dahlen F. A., Masters G., Engdahl E. R. and Hung S. H. (2004) Finite-frequency tomography reveals a variety of plumes in the mantle. *Science* **303**, 338–343.
- Moore L. R., Gazel E., Tuohy R., Lloyd A. S., Esposito R., Steele-MacInnis M., Hauri E. H., Wallace P. J., Plank T. and Bodnar R. J. (2015) Bubbles matter: An assessment of the contribution of vapor bubbles to melt inclusion volatile budgets. *Am. Mineral.* 100, 806–823.
- Mysen B. O., Eggler D. H., Seitz M. G. and Holloway J. R. (1976) Carbon dioxide in silicate melts and crystals; Part I, Solubility measurements. *Am. J. Sci.* **276**, 455–479.
- Neave D. A., Maclennan J., Edmonds M. and Thordarson T. (2014) Melt mixing causes negative correlation of trace element enrichment and CO₂ content prior to an Icelandic eruption. *Earth Planet. Sci. Lett.* **400**, 272–283.
- Newcombe M. E., Fabbrizio A., Zhang Y., Ma C., Le Voyer M., Guan Y., Eiler J. M., Saal A. E. and Stolper E. M. (2014) Chemical zonation in olivine-hosted melt inclusions. *Contrib. Mineral. Petrol.* **168**, 1030.
- Ni P., Zhang Y. and Guan Y. (2017) Volatile loss during homogenization of lunar melt inclusions. *Earth Planet. Sci. Lett.* 478, 214–224.
- Norman M. D. and Garcia M. O. (1999) Primitive magmas and source characteristics of the Hawaiian plume: petrology and geochemistry of shield picrites. *Earth Planet. Sci. Lett.* 168, 27– 44
- Pan V., Holloway J. R. and Hervig R. L. (1991) The pressure and temperature dependence of carbon dioxide solubility in tholeiitic basalt melts. *Geochim. Cosmochim. Acta* 55, 1587–1595.
- Pietruszka A. J., Norman M. D., Garcia M. O., Marske J. P. and Burns D. H. (2013) Chemical heterogeneity in the Hawaiian mantle plume from the alteration and dehydration of recycled oceanic crust. *Earth Planet. Sci. Lett.* 361, 298–309.
- Poland M. P., Miklius A. and Montgomery-Brown E. K. (2014) Magma supply, storage, and transport at shield-stage Hawaiian volcanoes. *U.S. Geol. Surv. Prof. Pap.* **1801**, 179–234.
- Rasmussen D. J., Kyle P. R., Wallace P. J., Sims K. W., Gaetani G.
 A. and Phillips E. H. (2017) Understanding degassing and transport of CO₂-rich Alkalic Magmas at Ross Island, Antarctica using Olivine-Hosted Melt Inclusions. *J. Petrol.* 58, 841–861.
- Roedder E. (1984) Fluid inclusions. In Rev. Mineral. 12. Washington: Mineralogical Society of America.
- Rosenthal A., Hauri E. H. and Hirschmann M. M. (2015) Experimental determination of C, F, and H partitioning between mantle minerals and carbonated basalt, CO₂/Ba and CO₂/Nb systematics of partial melting, and the CO₂ contents of basaltic source regions. *Earth Planet. Sci. Lett.* **412**, 77–87.
- Ryan M. P. and Sammis C. G. (1981) The glass transition in basalt. J. Geophys. Res. 86, 9519–9535.
- Ryan W. B., Carbotte S. M., Coplan J. O., O'Hara S., Melkonian A., Arko R., Weissel R. A., Ferrini V., Goodwillie A., Nitsche F. and Bonczkowski J. (2009) Global multi-resolution topography synthesis. *Geochem. Geophys. Geosys.* 10, Q03014.
- Saal A. E., Hauri E. H., Langmuir C. H. and Perfit M. R. (2002) Vapour undersaturation in primitive mid-ocean-ridge basalt and the volatile content of Earth's upper mantle. *Nature* 419, 451–455.

- Sano Y. and Williams S. N. (1996) Fluxes of mantle and subducted carbon along convergent plate boundaries. *Geophys. Res. Lett.* 23, 2749–2752.
- Shaw A. M., Hauri E. H., Fischer T. P., Hilton D. R. and Kelley K. A. (2008) Hydrogen isotopes in Mariana arc melt inclusions: Implications for subduction dehydration and the deep-Earth water cycle. *Earth Planet. Sci. Lett.* 275, 138–145.
- Shaw A. M., Behn M. D., Humphris S. E., Sohn R. A. and Gregg P. M. (2010) Deep pooling of low degree melts and volatile fluxes at the 85°E segment of the Gakkel Ridge: Evidence from olivine-hosted melt inclusions and glasses. *Earth Planet. Sci. Lett.* **289**, 311–322.
- Shimizu K., Saal A. E., Myer C. E., Nagl A. N., Hauri E. H., Forsyth D. W., Kamenetsky V. S. and Niu Y. (2016) Twocomponent mantle melting-mixing model for the generation of mid-ocean ridge basalts: implications for the volatile content of the Pacific upper mantle. *Geochim. Cosmochim. Acta* 176, 44– 80
- Shishkina T. A., Botcharnikov R. E., Holtz F., Almeev R. R., Jazwa A. M. and Jakubiak A. A. (2014) Compositional and pressure effects on the solubility of H₂O and CO₂ in mafic melts. *Chem. Geol.* **388**, 112–129.
- Sides I., Edmonds M., Maclennan J., Houghton B. F., Swanson D. A. and Steele-MacInnis M. J. (2014a) Magma mixing and high fountaining during the 1959 Kīlauea Iki eruption, Hawai'i. Earth Planet. Sci. Lett. 400, 102–112.
- Sides I. R., Edmonds M., Maclennan J., Swanson D. A. and Houghton B. F. (2014b) Eruption style at Kīlauea Volcano in Hawai'i linked to primary melt composition. *Nat. Geosci.* 7, 464–469.
- Sleep N. H. and Zahnle K. (2001) Carbon dioxide cycling and implications for climate on ancient Earth. J. Geophys. Res. 106, 1373–1399.
- Sobolev A. V. (1996) Melt inclusions in minerals as a source of principle petrological information. *Petrology* 4, 209–220.
- Sobolev A. V., Hofmann A. W., Sobolev S. V. and Nikogosian I. K. (2005) An olivine-free mantle source of Hawaiian shield basalts. *Nature* 434, 590–597.
- Steele-Macinnis M., Esposito R. and Bodnar R. J. (2011) Thermodynamic model for the effect of post-entrapment crystallization on the H₂O–CO₂ systematics of vapor-saturated, silicate melt inclusions. *J. Petrol.* **52**, 2461–2482.
- Trull T., Nadeau S., Pineau F., Polve M. and Javoy M. (1993) C-He systematics in hotspot xenoliths: Implications for mantle carbon contents and carbon recycling. *Earth Planet. Sci. Lett.* 118, 43–64.
- Tucker J. M., Mukhopadhyay S. and Gonnermann H. M. (2018) Reconstructing mantle carbon and noble gas contents from degassed mid-ocean ridge basalts. *Earth Planet. Sci. Lett.* 496, 108–119.
- Tuohy R. M., Wallace P. J., Loewen M. W., Swanson D. A. and Kent A. J. (2016) Magma transport and olivine crystallization depths in Kīlauea's east rift zone inferred from experimentally rehomogenized melt inclusions. *Geochim. Cosmochim. Acta* 185, 232–250
- Valbracht P. J., Staudigel H., Honda M., McDougall I. and Davies G. R. (1996) Isotopic tracing of volcanic source regions from Hawaii: decoupling of gaseous from lithophile magma components. *Earth Planet. Sci. Lett.* 144, 185–198.
- Walker J. C., Hays P. B. and Kasting J. F. (1981) A negative feedback mechanism for the long-term stabilization of Earth's surface temperature. J. Geophys. Res. 86, 9776–9782.
- Wallace P. J., Kamenetsky V. S. and Cervantes P. (2015) Melt inclusion CO₂ contents, pressures of olivine crystallization, and the problem of shrinkage bubbles. Am. Mineral. 100, 787–794.

- Wanless V. D. and Shaw A. M. (2012) Lower crustal crystallization and melt evolution at mid-ocean ridges. *Nat. Geosci.* **5**, 651–655.
- Wanless V. D., Behn M. D., Shaw A. M. and Plank T. (2014) Variations in melting dynamics and mantle compositions along the Eastern Volcanic Zone of the Gakkel Ridge: insights from olivine-hosted melt inclusions. *Contrib. Mineral. Petrol.* 167, 1005.
- Wanless V. D., Shaw A. M., Behn M. D., Soule S. A., Escartin J. and Hamelin C. (2015) Magmatic plumbing at Lucky Strike volcano based on olivine-hosted melt inclusion compositions. *Geochem. Geophys. Geosys.* 16, 126–147.
- Watson E. B., Sneeringer M. A. and Ross A. (1982) Diffusion of dissolved carbonate in magmas: experimental results and applications. *Earth Planet. Sci. Lett.* 61, 346–358.

- Wolfe C. J., Solomon S. C., Laske G., Collins J. A., Detrick R. S., Orcutt J. A., Bercovici D. and Hauri E. H. (2009) Mantle shearwave velocity structure beneath the Hawaiian hot spot. *Science* **326**, 1388–1390.
- Weis D., Garcia M. O., Rhodes J. M., Jellinek M. and Scoates J. S. (2011) Role of the deep mantle in generating the compositional asymmetry of the Hawaiian mantle plume. *Nat. Geosci.* **4**, 831–838
- Zhang Y. and Zindler A. (1993) Distribution and evolution of carbon and nitrogen in Earth. *Earth Planet. Sci. Lett.* **117**, 331–345

Associate editor: Rajdeep Dasgupta